Accepted Manuscript

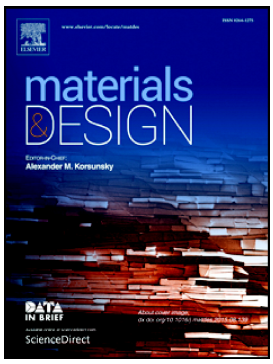

Sinter structure analysis of titanium structures fabricated via binder jetting additive manufacturing

Evan Wheat, Mihaela Vlasea, James Hinebaugh, Craig Metcalfe

PII:	S0264-1275(18)30505-7
DOI:	doi:10.1016/j.matdes.2018.06.038
Reference:	JMADE 4008
To appear in:	*Materials & Design*
Received date:	12 February 2018
Revised date:	26 May 2018
Accepted date:	20 June 2018

Please cite this article as: Evan Wheat, Mihaela Vlasea, James Hinebaugh, Craig Metcalfe , Sinter structure analysis of titanium structures fabricated via binder jetting additive manufacturing. Jmade (2018), doi:10.1016/j.matdes.2018.06.038

Sinter Structure Analysis of Titanium Structures Fabricated via Binder Jetting Additive Manufacturing

Evan Wheat[1], Mihaela Vlasea[1], James Hinebaugh[2], Craig Metcalfe[2]

1-University of Waterloo, Department of Mechanical and Mechatronics Engineering, Waterloo, Ontario, N2L 3G1

2-Expanse Microtechnologies Inc., Toronto, Ontario, M4R 2H8

Submitted Electronically to: Journal of Materials & Design

Note to Journal Editor: The manuscript describes the in-depth relationship between the principles of sintering mechanisms, the theory of thermodynamics and kinematics of sintering, and process outcomes for binder jetting additive manufacturing.

Revision Date: May 5, 2018

Number of Pages: 38

Number of Figures: 18

Number of Tables: 8

Corresponding Author: Mihaela Vlasea, PhD, Assistant Prof.

Address: Department of Mechanical and Mechatronics Engineering, University of Waterloo, Waterloo, ON, N2L 3G1 Canada, e-mail: mihaela.vlasea@uwaterloo.ca

Abstract:

To facilitate functional part production in metal binder jetting additive manufacturing, the relationship between materials, process and sintering needs to be understood. This work relates sintering theory with process outcomes. For this, commercially pure titanium was deployed to study the effect of powder size distributions on green and sintered part qualities (bulk density, relative density, particle size, pore size, sinter neck size). The powders were uni- and bi-modal blends of 0-45 µm, 45-106 µm, and 106-150 µm. Computed tomography analysis was used to evaluate non-densifying (1000 °C) and densifying (1400°C) sintering regimes. For green parts, the relative density and powder size distribution along the build direction followed a periodic fluctuation equivalent to the 150 µm layer thickness. The relative density fluctuation range was higher (±20 %) for bi-modal blends with 0-45 µm, compared to all other blends (±8 %) due to powder segregation. For non-densifying sintering, parts with 0-45 µm blends displayed both densifying and non-densifying behavior. For densifying sintering, powders containing 0-45 µm blends surpassed the 70% density threshold expected for this sintering regime. Overall, the finer particles improved bulk density of sintered parts, at the expense of higher levels of shrinkage and density anisotropy along the build direction.

Key words:

Additive manufacturing; binder jetting; computed tomography; commercially pure titanium powder blends; sinter structure analysis; particle distribution

1 Introduction

Additive manufacturing (AM) has recently seen a significant amount growth in both its use and capabilities, with an increased adoption in industrial, commercial and consumer markets [1]. There are a few major benefits to this layer-by-layer manufacturing approach. The first is that there is little to no material waste since, apart from support structures, the only material consumed during the build process is that which actually makes up the part. In theory, this should reduce the raw material costs of the part. This may not always hold true, since materials for AM systems can be significantly more expensive than those used in traditional processes [2,3]. Another recognized benefit is that there is no specific tooling required to fabricate parts, thus the lead time to production can be shortened. Another benefit of AM is the ability to create

exceptionally complex parts that could not be made using traditional means. Design freedom also enables consolidation of assemblies into fewer parts.

One of the major categories of AM is binder jet AM (BJAM). BJAM, also referred to as 3D printing and powder-bed binder-jet (PBBJ) AM, was developed at the Massachusetts Institute of Technology in the late 1980's and early 1990's and patented in 1993 [4]. In BJAM, the layer slices from the CAD file are converted into images, which are printed onto a powder bed with a liquid-state binder using a print head. This binder consolidates the powder within and between layers. Once the printing is completed, the part can be used as-is, cured, infiltrated or sintered. The benefit BJAM has over other AM processes is that the fabrication system can be deployed for manufacturing metallic [5–18], ceramic [19–26] and polymer [27,24,19] parts. In addition, BJAM systems typically cost significantly less than other metal AM systems and have lower operating costs [28], lowering the barrier to adoption of the process. For other metal AM processes such as laser powder bed fusion (PBF), the systems have restrictive build sizes and can take significantly longer than BJAM to make parts of any appreciable size [24].

AM processes have migrated towards producing functional components. For metal AM, this shift to functional part production has been facilitated by a greater understanding of the materials and processes involved and how they affect the qualities of the final parts. BJAM has seen considerably less research and development compared to other metal AM processes, specifically in terms of expanding the range of deployable materials, development of process predictive models, and optimization of process parameters. This lack of development may be attributed to the inherent porosity present in BJAM parts. While porosity is highly desirable in many applications such as medical [29,30], dental [31,32], light-weighting [24], filtering [33] and many others, it is detrimental in many industrial applications. Porosity needs to be controlled to ensure part properties are optimal for the desired application. Without a means to control porosity or predict final part properties, BJAM will continue to see lower levels of industrial adoption for production of metallic functional components. Though not as prevalent in its use, many different metallic or metallic-based materials have been used in BJAM to directly fabricate parts. One of the more prevalent materials are stainless steels, mainly 316L [5–8] and 420 [9]. Work has also been reported on producing parts with materials as diverse as magnetic materials [34,13,14], titanium [15,16], copper [17], Inconel 625 [10–12], and cobalt-chrome [18].

The motivation behind this work is the desire to see a more widespread industrial adoption of BJAM, with a direct application in fabrication of biomedical titanium bone and dental augmentation segments. The inherent porosity seen in BJAM parts can be greatly beneficial for many medical applications. Many medical implants [29,30] and dental restorations [32,35] require bio-mimetic porous architectures and patient-specific design strategies. Currently these parts are difficult or expensive to manufacture. PBBJ presents a commercially viable opportunity to address the limitations in this space. Being able to predict final part properties is critical to manufacture such parts with a high degree of repeatability and accuracy, as well as to enable fast adoption of BJAM technologies in this field. Commercially pure (CP) titanium was chosen as the material of interest in this study because it is bio-compatible and certified for both orthopedic and dental parts, furthermore the material is also used for high value components in other areas of application, and lastly, this work advances the existing research on BJAM of titanium [15,16].

The focus of this work is to study the effects of different powder types (sizes and distributions) on the green and sintered part densities, and to further the understanding of the driving mechanisms behind the development of the sinter structure. Understanding how different powders and sintering strategies affect density, and subsequent part properties, is crucial to tailor parts to specific applications. To this effect, density measurements through computed tomography (CT) are used to evaluate the effects of the different powder types on both bulk and localized density under two sintering regimes, non-densifying and densifying. The interpretation of results is dependent on the understanding of sintering theory, which is described below.

1.1 Stages of Sintering

The BJAM process produces a component held together with binder, typically referred to as a green part. To achieve titanium components with suitable mechanical properties, the green part must be sintered. The sintering process connects the titanium particles with metallic bonds through a diffusion process, giving strength and changing the density of the final part. Final part density is closely linked to static and dynamic mechanical properties. Sintering is fundamentally based on the reduction of surface energy of the system. There are three stages of sintering, initial, intermediate and final (Figure 1), each producing parts with distinct morphologies.

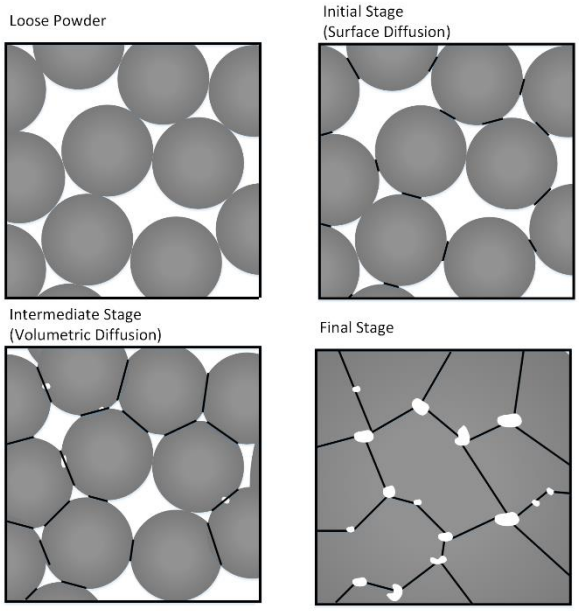

Figure 1: Schematic showing the general sintering process for a powder system: un-sintered (loose powder), initial stage, intermediate stage and final stage; adopted from [36]

The initial stage of sintering occurs at lower temperatures and is dominated by surface diffusion [37]. At the start of the initial stage, there are no sinter necks present and the part will be at its green density. For titanium parts made by BJAM, green density is typically in the range of 50%-60% dense or higher, depending on the process parameters and powder size distribution chosen. During the initial stage, material migrates on the surface of the particles to contact points, creating sinter necks [37], as shown in Figure 1. There is little dimensional change in parts during the initial stage with linear shrinkage being around 3% [36]. The part moves past the initial sinter stage once the sinter necks are approximately 1/3 the diameter of the particles [36]. This usually occurs when the part is approximately 60% to 70% of its theoretical density [38,39].

After the initial stage, the parts enter the intermediate sinter stage. The intermediate stage occurs at higher temperatures, with the specific temperature being determined by the material and particle size. The mechanisms present in this stage are dominated by volumetric diffusion. During the intermediate stage, a significant amount of densification occurs. The part will go from being 70% to approximately 92% of its theoretical density [38,40]. During the intermediate stage the pores of the part are initially smoothened, becoming more tubular, in contrast to the spherical pores seen in the initial stage [36,38]. Sinter necks grow from approximately 1/3 to 1/2 of the particle diameter and as densification progresses, the long, tubular pores become closed [37].

Once the pores are closed (sinter necks are 1/2 of the particle diameter and parts 92% dense), the part has entered the final sinter stage. The final sinter stage takes place in the same temperature range as the intermediate stage and similar sinter mechanisms are present. During this stage the enclosed pores are eliminated, if possible, and the part will achieve its maximum possible density. Since the titanium parts are usually sintered in argon atmosphere with pressure slightly above atmospheric, 100% density is not possible to achieve [41]. During the final sinter stage, the grain structure within the part coarsens significantly as well [37].

1.2 Thermodynamics of Sintering

The driving force for the sintering process is the reduction in energy of the system. At any interface, titanium atoms are not fully bonded, causing them to be in a higher energy state [36]. The reduction in energy of the system occurs by reducing the number of atoms in a higher energy state. Sintering continues as long as the total energy in the system is decreased and stops once that is no longer possible. During the initial stage of sintering, necks form between adjacent particles. There is a large driving force to generate necks due to the effects of surface curvature, κ [38]. When a surface has curvature there is an uneven distribution of forces on the atoms causing the surface to be in tension if it is concave and compression if it is convex [36]. As the sinter necks form, the total curvature of the surface is reduced, reducing the system energy. When a surface is under tension or compression, the surface will respectively have a higher and lower vacancy concentration [36]. This difference in vacancy concentrations causes a source-sink relationship, where material from the particles preferentially moves to the necks [40]. Equation 1 describes the relationship between capillary stress (σ) in a sinter neck as being proportional to the surface energy of the particles (γ) and the inverse of the particle radii (r_1, r_2 - for particles 1 and 2). With smaller radii, particles will have a higher curvature, and therefore a higher driving force for sintering. This in turn means that the powder system requires less energy for sintering to occur. Smaller particles have a significantly higher stress, and therefore driving force for sintering. While Equation 1 is specific for stress in a sinter neck, many of the driving forces based on particle geometry are proportional to the inverse of the particle radii and show a similar trend [36].

$$\sigma = \gamma\kappa = \gamma\left(\frac{1}{r_1} + \frac{1}{r_2}\right) \qquad \text{Equation (1)}$$

$$SA{:}V = \frac{4\pi r^2}{\frac{4}{3}\pi r^3} = \frac{3}{r} \qquad \text{Equation (2)}$$

In addition to reducing surface curvature, the formation of necks also reduces the surface area to volume ratio of the powder system (SA:V), described by Equation 2. The SA:V ratio is directly proportional to the inverse of the particle radii (r). As the size of the particles increases, the total surface area of the powder system decreases, decreasing the system energy. This contributes to the lower energy required for sintering of smaller particles as the comparatively high surface area to volume ratio gives the system a higher driving force for sintering [42].

1.3 Kinematics of Sintering

There are three major categories of sintering mechanisms, all of which can be active in some combination during the sintering process. The relative impact of each mechanism depends on the material and sintering conditions. The main categories are solid-state, liquid and viscous sintering. Solid-state sintering occurs with the material in its solid form, and diffusion controlled mechanisms dominate the process. In liquid sintering, some volume of liquid is present, typically in small amounts, which facilitates the sintering process [43]. Viscous sintering, somewhat similar in concept to liquid sintering, occurs in amorphous materials where the material can flow, but is not considered to be a fluid [44]. For this work, liquid and viscous sintering mechanisms have a negligible effect (if present at all) on the sintering of CP titanium [45] and therefore solid-state sintering is the focus of the following sections.

The mechanisms that occur in solid-state sintering are predominantly based on atomic diffusion. Within the category of solid-state sintering, there are two distinct types of sintering mechanisms that contribute in different ways to the sintering process. The first type is coarsening or non-densifying sintering. These mechanisms typically occur at lower temperatures and are comprised of surface effects [46]. The other type is volumetric or densification sintering, which occurs through mass transfer, grain boundary diffusion, and plastic flow as described below. These mechanisms occur at higher temperatures and cause shrinkage in parts [46]. Both non-densifying and densifying mechanisms can occur at the same time, and the prevalence of each one depends on the sintering temperature.

1.3.1 Non-Densifying Sintering Mechanisms

Non-densifying or coarsening sintering are mechanisms that do not cause the centers of particles to move closer together. Instead, material is redistributed along the particle surface from convex to concave areas [46], as shown in Figure 2. Since material is not moved from the core of the particle, there is no appreciable shrinkage of the part. Rather the structure is smoothed (also referred to as coarsened) to reduce surface curvature and surface area. The main mechanism that causes this is surface diffusion. Surface diffusion is simply the movement of atoms along the surface of the particle. This mechanism occurs at the lowest temperatures of any of the mechanisms, due to the comparatively high energy of particles on the surface [37] and lower activation energy [47]. The other mechanism that causes coarsening is evaporation and condensation. Through this mechanism, material will evaporate at convex areas and condense at concave areas due to a higher and lower vapor pressure at those areas respectively [48], allowing material to be transferred across pores rather than on or through the particles themselves. The effects of this mechanism are typically considered negligible for most materials since the vapor pressure is low at any realistic sintering temperature [46]. Titanium has a relatively high vapor pressure compared to other metals, thus effects of evaporation-condensation are likely minimal.

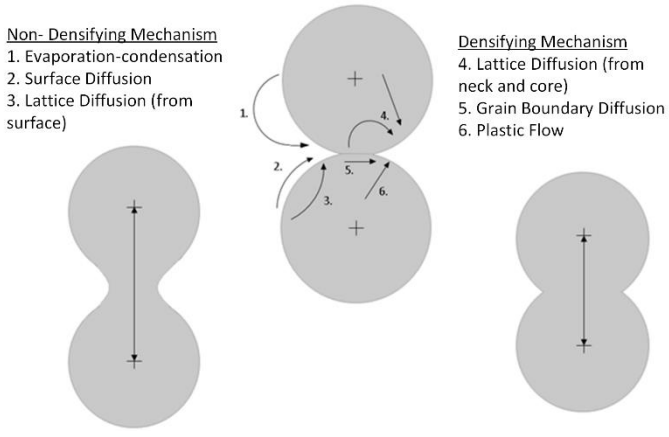

Figure 2: Possible solid-state sintering mechanisms, including non-densifying mechanisms (left) and densifying mechanisms (right)

1.3.2 Densifying Sintering Mechanisms

In densifying sintering, mass from the particles will move from the core of the particles to the necks [46]. This movement of mass causes the centers of the particles to move closer together, as shown in Figure 2, causing shrinkage during the sintering process. The first

mechanism to cause this is the lattice or volumetric diffusion. This occurs in CP titanium as self-diffusion, where the process is caused by vacancies in the lattice structure. The base number of vacancies in the lattice is directly proportional to temperature. The mechanism is only active at higher temperatures (typically above 1100°C) due to the requirement of a large number of vacancies to provide any meaningful mass flow [46].

The other prominent densifying mechanism is grain boundary diffusion. Grain boundary diffusion occurs at lower temperatures compared to volumetric diffusion since it does not rely on the creation of vacancies, with atoms being able to take advantage of the space provided by grain boundary interfaces. Atoms will diffuse from grain boundaries inside the particle to the surface of the particle. The effect is the same as volumetric diffusion though the mechanism is dependent on the quantity of grain boundaries as well as temperature [38].

The final mechanism that causes densifying sintering is plastic flow, occurring by the movement of dislocations in the lattice structure. For the mechanism to actually cause densifying sintering, the dislocation must occur at the surface and move inwards to either a grain boundary or isolated pore [46]. There is some evidence that the surface stresses from surface curvature generate enough stress to form dislocations, but the total effect of the mechanism is uncertain [46]. This mechanism can only occur at lower temperatures, since at elevated temperatures the part is effectively being constantly annealed, preventing dislocations from forming.

For CP titanium, and most metals in general, the only mechanisms that truly cause densifying shrinkage to any appreciable degree are volumetric and grain boundary diffusion [46]. It is important to note that it is the powder system and geometry that determines where material diffuses to. Material properties and temperature only determine how the material diffuses.

2 Materials and Methods

2.1 Material System used in Additive Manufacturing of Parts

2.1.1 Titanium Powder Materials

For this work, all titanium powders used were plasma atomized, Grade 1 commercially pure (CP) titanium (Advanced Powders and Coatings, Canada). Three stock powder size ranges

were purchased for the production of samples. Two size distributions, 0-45 µm (●○○) and 45-106 µm (○●○), were used in an unaltered, as-purchased state. The third size distribution, 75-250 µm, was sieved to remove particles larger than 150 µm and less than 106 µm, using 100 and 140 mesh sizes respectively (U.S.A Standard Test Sieve - Brass, Cole-Parmer, USA), to make a 106-150 µm (○○●) size distribution. The sieving was carried out on a mechanical sieving system conforming to ASTM C136 (model D-4325, Dual Manufacturing Co., USA). The five different powder types used to produce samples are listed in Table 1. Two mono-modal powders (Types B ○○● and C ○●○), as well as three bimodal powders (Types A ○●●, D ●○● and E ●●○) were used in the production of samples. The three bi-modal powder distributions were made by blending the three mono-modal distributions at equal weight ratios. Weight measurements for making the bi-modal compositions was done using a precision balance (APX-203, Denver Instruments, USA). The mono-modal 0-45 µm powder was not used for the production of samples at the time due to powder spreadability concerns.

Table 1: Titanium powder size combinations, with powder blends at equal weight ratios. For instance, Type B ○○● only has 106-150 µm in the blend, while Type A ○●● has a blend of 45-106 µm and 106-150 µm.

Powder Designation	Powder Size Composition (µm)
Type A ○●●	45-106/106-150
Type B ○○●	106-150
Type C ○●○	45-106
Type D ●○●	0-45/106-150
Type E ●●○	0-45/45-106

The chemical composition of the three purchased mono-modal powders conforms to ASTM B348 for a Grade 1 CP titanium powder. The chemical composition titanium powder type and the relevant testing standard for each element is listed in the associated Data in Brief.

2.1.2 Polyvinyl Alcohol Powder Material

Polyvinyl alcohol (PVA) was used as the solid state binder for the production of samples. The PVA used was a low molecular weight, 86-89 % hydrolyzed polymer (Alfa Aesar, Ward Hill, MA). The material in its as-purchased condition was in the form of large, irregular particles that could not be used in the BJAM process. The purchased PVA powder was ground using a blade grinder and was sieved to be less than 63 µm in size using a 230 standard US mesh brass sieve (U.S.A Standard Test Sieve - Brass, Cole-Parmer, USA).

2.1.3 Liquid Binder Material

The liquid binder used to print parts was the standard ZB60 liquid binder produced by 3D Systems (3D Systems, NC, USA). While the exact composition of the material is not provided, the binder is an aqueous solution (approximately 85%-95% water) with some additional polymers as binding agents. From previous works done on the printing of titanium powder, this liquid binder was found to bind well with the CP titanium particles in the green state [15].

2.1.4 Powder Material Blend Preparation

The powder used for printing was made by mixing each of the five titanium powder blends with the PVA powder. The PVA powder was added to make a mixture with a composition of 3 wt% PVA, with the weighing done using a precision balance (APX-203, Denver Instruments, USA). Mixing was carried out using a previously developed process [15] that entailed placing the titanium and PVA powders in a jar and rotating the mixture on a jar-mill (Labmill 8000, Gardco, USA) at 128 rpm for 4 hours.

2.2 Additive Manufacturing of Parts

All samples were produced using modified 310Plus (Z Corporation - acquired by 3D Systems, NC, USA). Inserts were made and installed to reduce the effective build bed and feed bed size of the system to 32x32x50 mm xyz respectively. An illustration of the reduced build bed configuration is shown in the Data in Brief. The print file consisted of 16 cylinders, each 5 mm in diameter and 8 mm in height, placed in a 4 by 4 array, at 6.5mm center to center distance. Printing parameters, shown in Table 2, were identical for all samples to be able to isolate the effects of different powder types. The effects of printing parameters has already been explored elsewhere [15,16]. A layer thickness of 150 µm was chosen since that is the smallest layer thickness that accommodated the largest particle size range. The enclosure temperature was used from previous works [15], enabling the appropriate rate of evaporation of the liquid binder.

Table 2: BJAM printing parameters used in the ZPrint software for sample production

Parameter	Value
Layer thickness	150µm
Shell binder amount	100%
Core binder amount	200%
Enclosure temperature	40°C
Drying time (after printing)	1 hour

2.3 Sintering Parameters

Two different sintering schedules were used to sinter parts either in the non-densifying or densifying domain. The specific schedules for non-densifying and densifying sintering are shown in Figure 3. All sintering was carried out using a high-temperature tube furnace (GSL—1500X-50, MTI Corporation, USA), with samples placed uncovered in high purity alumina crucibles (EQ-CA-L100W20H20, MTI Corporation, USA). Binder burnout was carried out in air while sintering was carried out under a high-purity argon atmosphere. The samples were brought back down to room temperature after binder burnout to be able to attach the end caps on the tube furnace to seal the system for sintering under an argon atmosphere.

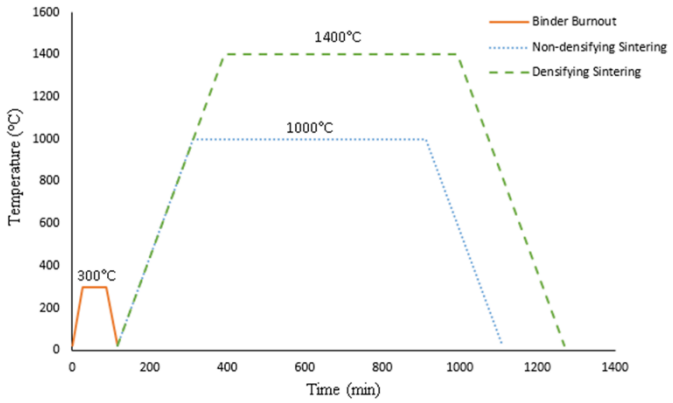

Figure 3: Sintering schedule for densifying and non-densifying sintering. Binder burnout was carried out in air, while sintering was carried out in argon

Hold temperatures for sintering were chosen as 1000 °C and 1400 °C for non-densifying and densifying sintering respectively. Sintering of titanium only begins in any substantial way above the alpha-beta transition temperature, approximately 880 °C [45]. The 1000 °C temperature was chosen to be slightly above that minimum temperature to allow sintering to occur at a reasonable rate but to ideally only allow non-densifying sintering mechanisms to be active. The 1400 °C temperature was the highest continuous sintering temperature possible in the furnace. While limited by the capabilities of the furnace, this temperature (268 °C below melting) was deemed sufficiently high to perform densifying sintering. A hold time of 10 hours was chosen to ensure the two types of sintering had proceeded sufficiently enough for analysis.

2.4 Sinter Structure Analysis

An experiential procedure was carried out to understand the sinter structure effects from densifying and non-densifying sintering. Ten samples were used as part of the analysis, being evaluated in both a green and sintered state in terms of porosity, sinter neck size, pore size and particle size using computed tomography (CT). A summary of the parts and their respective sinter schedules is shown in Table 3. The green sample masses were compensated for the assumed 3wt% of PVA mass to only indicate the expected mass of Ti in the sample. The differences between the green and sintered mass is negligible for most samples though a number of the samples show a change in mass after sintering. The difference in mass could be due to inconsistent powder mixing, meaning the sample did not consist of exactly 3wt% PVA. With more or less PVA in the green sample, the sintered sample would be expected to show a decrease or increase in mass respectively. In addition, a number of samples showed surface oxidation after sintering, with powder Types D ●○● and E ●●○ showing the most. The surface oxidation of the sample would also contribute to minor mass gains after the sintering process.

Table 3: Sample summary for sinter structure analysis. The CT samples are identified with A, B, C, D and E as the part powder type and H and L representing the 1400℃ and 1000°C sintering regime respectively

Sample	Powder	Compensated Green Mass (g)	Sintered	Max Sintering Temperature (°C)
CT-AL	Type A ○●●	0.455	0.456	1000
CT-AH	Type A ○●●	0.441	0.447	1400
CT-BL	Type B ○○●	0.460	0.461	1000
CT-BH	Type B ○○●	0.456	0.455	1400
CT-CL	Type C ○●○	0.390	0.391	1000
CT-CH	Type C ○●○	0.386	0.393	1400
CT-DL	Type D ●○●	0.380	0.404	1000
CT-DH	Type D ●○●	0.443	0.450	1400
CT-EL	Type E ●●○	0.377	0.377	1000
CT-EH	Type E ●●○	0.364	0.380	1400

2.4.1 Micro-scale Computed Tomography Method

The CT scanning (Xradia 520 Versa, Zeiss, USA) was performed using the same parameters (see Table 4) for both the green and sintered parts. Due to operator error, samples CT-CL and CT-CH, while in the green state, were scanned at 3.716µm. CT-CL and CT-CH in the sintered state and all other samples were scanned at 3.807µm. This difference in voxel size was accounted for in subsequent analysis. Reconstruction was completed using the Zeiss

Reconstruction software to produce gray-scale 16-bit images. Subsequent image processing of was performed using ImageJ. A single set of byte scaling factors were applied to normalize the 16-bit intensity values to an 8-bit range. Then, an edge preserving bilateral filter was applied (spatial radius of 2 voxels and intensity range of 50) to normalize the noise in the reconstructed images. Details on part alignment are described in the associated Data in Brief.

Table 4: Scout-and-Scan settings used for CT scanning

Parameter	Value
Source power	10W
X-ray energy	120kV
Filter	HE1
X-ray optic	4x lens
Exposure time	1.5s
Number of projections	1201
Binning level	2
Voxel size (approximate)	3.8µm

Segmentation of CT images was done using the sample mass and material density. Based on titanium density value of 4.506g/cm^3, the segmented sample volumes were multiplied by the density to obtain the sample mass. The mass was assumed to be 97 %wt and 100 %wt titanium for the green and sintered parts respectively. Due to the significantly lower attenuation value of PVA, the PVA was not visible in any of the gray-scale images. Thresholding values of 138 and 143 were found for the green and sintered parts respectively. Figure 4 shows a gray-scale slice of the CT-AH ○●● green part and corresponding segmented image.

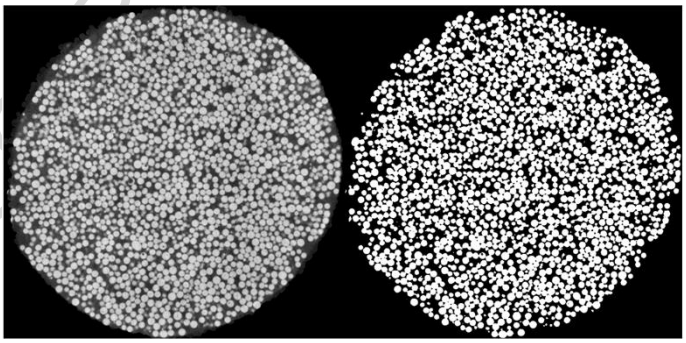

Figure 4: Gray-scale (left) and segmented image (right) of a slice of the CT-AH ○●● green part

2.4.2 Region of Interest Position and Size

For this work, the CT analysis was performed on a single replicate of each of the powder Types A ○●●, B ○○●, C ○●○, D ●○● and E ●●○ at 1400°C (H) and 1000°C (L) sintering regime respectively. Analysis of the CT image sets consisted of finding relative density, particle size, pore size and sinter neck size. All values were found on a per-layer basis, with the average giving the overall value for the entire part. It was determined to be unfeasible to analyze the entirety of each sample, therefore, a 1.25mm x 1.25mm x 2.25mm ROI was used for the green samples. The sensitivity to ROI size and location is presented in the associated Data in Brief, with deviations of under 1%, which were deemed acceptable. The ROIs were scaled equal to the amount of shrinkage seen in each sample after sintering to capture the same particles in the analysis. The long axis of the ROI was aligned parallel to the build direction (Z axis) to be able to better capture a larger number of layers in the analysis. The relative density was calculated by comparing the area of the particle space (found by segmentation), to that of the overall layer.

2.4.3 Pore Size, Particle Size, and Sinter Neck Size Calculation

Pore size was found by segmenting the 3D pore volume into individual pores respectively, using the watershed-based technique of pore network extraction, first described in [49]. The resulting networks contained pore diameter, volume, and position, as well as the diameter of constrictions (throats) between neighboring pores. Pore diameters were calculated as the maximal inscribed sphere, and throat diameters were calculated as the size of the largest sphere that could travel between neighboring pores. Particle size was found through the same means as was used to find pore size, but with the reverse segmentation of the domain being used. Sinter neck diameter was found by analyzing the measured constriction diameters in the resulting particle networks. An unexpected result was that sinter necks of 0-40 μm range were measured for samples in the green state, when no such necks would have had the chance to form. These necks were measured because the air-gap between two merely touching spheres stays within 2 voxels for a considerable fraction of the particle height, and therefore could easily be improperly segmented into a sinter neck. Any sinter neck measurements below 50 μm should be treated as unreliable, as air gaps of less than 2 voxels often get lost in the segmentation process. Therefore, only qualitative sinter neck analysis was reported.

2.5 Statistical analysis

A differential scanning peak-finding algorithm was used to detect all peaks and valleys for all Z axis relative density plots. Each dataset was traversed and all points with zero relative density change along Z were identified. Points which were within 6.25% full-scale of the mean of the dataset were discarded. All minima above the mean of the data set and all maxima below the mean of the dataset were discarded. The local maxima were further filtered by only selecting maxima with the largest local value within two minima and vice-versa for local minima. The remaining maxima and minima were considered valid peaks and valleys within the dataset.

3 Results and Discussion

Quantitative sinter neck size results were found to be unreliable at the scanning resolution chosen for this study; in this context, a qualitative analysis of sinter necks is presented based on representative CT images. Quantitative results are only presented for porosity, pore size and effective particle size. Samples were sintered at both high (H) and low (L) temperatures to be able to see the combined effects of powder size and the two main groups of sintering mechanisms (densifying and non-densifying). An example of the overall reconstruction for CT-AL○●● before and after sintering is shown in Figure 5.

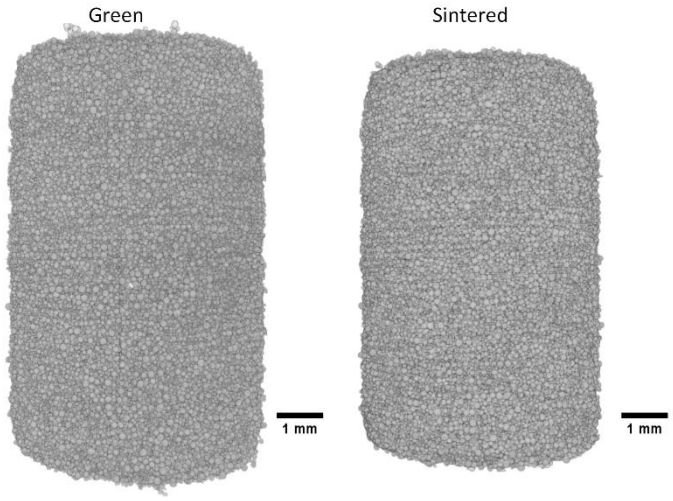

Figure 5 Orthogonal view comparison between sample CT-AL○●● in the green (left) and sintered (right) state, for a non-densifying sintering regime (up to 1000 °C)

3.1 Overall Relative Density

The bulk porosity results of the samples in both the green and sintered state are summarized in Table 5. All samples of the same powder type show essentially the same green density apart from samples CT-DH ●○● and CT-DL ●○●, which have a difference in green density of 4.9%. This difference is likely due to inconsistencies either in the actual powder distribution that makes up the respective parts or in the printing process by way of inconsistent spreading or jetting. The general trend seen with the samples is that as the average particle size decreases, so does the green density. Powder Type B ○○● gives samples with the highest green density, followed by Type A ○●●, Type D ●○●, Type C○●○ and finally by Type E ●●○, giving the lowest green density. This trend is likely due to the number of contact points in the various powder systems and compaction forces during printing. Since all of the parts were printed on the same system with the same settings, all of the parts would have undergone the same applied compaction forces during printing. However, due to the variation in powder sizes, the friction and inter-particle electrostatic forces in the different powder systems are not the same. Powder systems with smaller particles have more contact points, making the powder more resistive to applied forces due to friction as well as being more susceptible to electrostatic forces [17,37,40]. Therefore, with the same applied compaction forces (in this case from a roller on the 310Plus system), but with larger friction forces, it was expected that the powder systems with smaller particles would see lower green density levels. The trend seen from these results is similar to that seen in other works [9,17,50]. These results are not indicative of the maximum achievable green density for each powder type since powder spreading was not optimized for each powder type.

Table 5: Summary of the bulk densities of the CT sample ROIs in the green and sintered state

Sample Name	Green Density (%)	Sintered Density (%)	Density Change (%)
CT-AL ○●●	54.8	57.7	2.9
CT-AH ○●●	54.4	64.6	10.2
CT-BL ○○●	58.3	59.1	0.8
CT-BH ○○●	57.6	71.5	13.9
CT-CL ○●○	49.6	53.5	3.9
CT-CH ○●○	47.9	70.5	22.6
CT-DL ●○●	48.1	60.3	12.2
CT-DH ●○●	53.0	84.6	31.6
CT-EL ●●○	45.5	57.2	11.7
CT-EH ●●○	45.9	82.7	36.8

As expected, the parts sintered at 1000°C underwent significantly less densification compared to the parts sintered at 1400°C. It was expected that the samples sintered at 1000°C would only undergo non-densification sintering and therefore have a maximum shrinkage of around 3%. It was also expected that the parts sintered at the lower temperature would remain in the initial stage of sintering where only non-densifying sintering occurs. From the CT results, it can be seen that this is only true for samples CT-AL ○●●, CT-BL ○○● and CT-CL ○●○, which showed shrinkage levels of 2.9%, 0.8% and 3.9% respectively. For these samples, the sinter necks generally appeared to stay below the 1/3 the particle diameter threshold, as shown in Figure 6. Based on sinter neck size and the level of density change, all three of the samples remained within the initial stage of sintering, and only underwent non-densifying sintering.

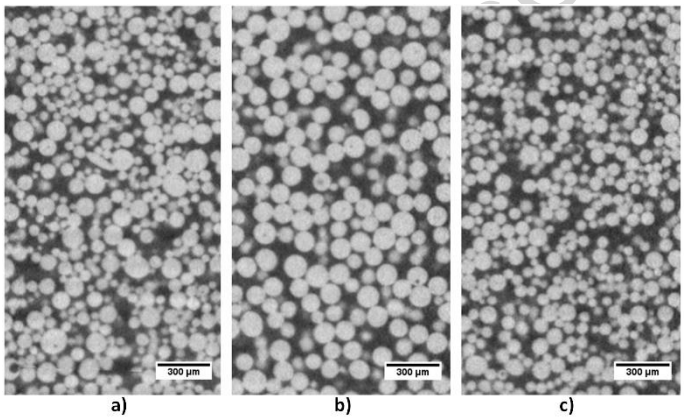

Figure 6: XZ plane cross-section images from reconstructed CT data of samples (a) CT-AL ○●●, (b) CT-BL ○○●, and (c) CT-CL ○●○ in the sintered state showing a qualitative view of the sample sinter necks between particles in the ROI

As discussed earlier, the energy required for sintering decreases exponentially with particle size, for both densification and non-densification sintering. This expected trend is confirmed for the shrinkage levels seen in the samples with CT-BL ○○● showing the lowest and CT-CL ○●○ the highest level of densification of the parts that underwent only non-densifying sintering. The minimal density changes of samples CT-AL ○●●, CT-BL ○○● and CT-CL ○●○ demonstrate that the titanium parts can be sintered with minimal dimensional change but still have sinter necks large enough to be distinguished within the powder system. A minimum dimensional change during sintering means less dimensional compensation of the part size during printing. If the green part density can be made high enough to be suitable for a specific application, the parts could be sintered at this lower temperature, minimizing need for any form of dimensional compensation.

Both CT-DL ●○● and CT-EL ●●○ samples showed significant levels of densification of 12.2% and 11.7% when sintered at 1000°C, indicating the parts underwent densification sintering. This higher level of shrinkage is due to the addition of the fine particles (0-45µm) that require significantly less energy for sintering. Based on the sinter neck sizes of the samples, shown in Figure 7, the sample appears to have undergone both densifying and non-densifying sintering, but with each localized to the fine (0-45µm) and larger (45-106µm and 106-150µm) particles groups respectively. From Figure 7, the sinter necks between the larger particles is comparable to those seen in samples CT-AL ○●●, CT-BL ○○● and CT-CL ○●○, indicating only non-densifying sintering. The relative size of the sinter necks seen between the smaller particles is significantly larger. Most of the particles show sinter necks larger than the 1/3 diameter ratio, indicating they have progressed, at least locally, into the intermediate sintering stage where significant densification occurs. This indicates that the majority of the shrinkage seen in the sample was caused by the smaller particles which undergo densifying sintering even at 1000°C.

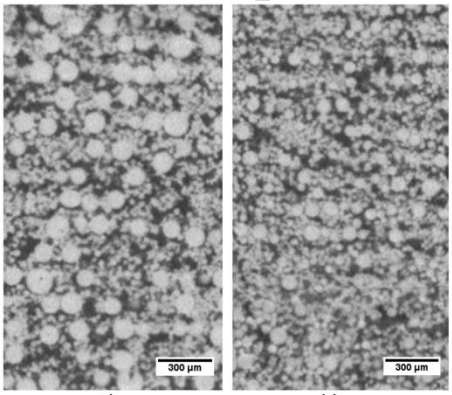

Figure 7: XZ plane cross-section images from reconstructed CT data of samples (a) CT-DL ●○●, and (b) CT-EL ●●○ in the sintered state showing a qualitative view of the sample sinter necks between particles in the ROI

The sinter results seen for CT-DL ●○● and CT-EL ●●○ are important for two reasons. First, any addition of very fine particles can cause unanticipated levels of shrinkage. The blending of large and very fine particles is theoretically, if powders are optimally spread, a suitable means of achieving high green density [9,50]. However, this may be detrimental if the intent is to have minimal shrinkage after sintering. Secondly, the addition of fine particles allows for sintering at comparatively low temperatures due to their lower activation energy. This enables for a more economical sintering with similar densification results, as low-temperature furnaces are more common and less expensive than similarly sized high-temperature ones.

The parts sintered at 1400°C underwent much higher levels of shrinkage during sintering. All of the parts underwent signification levels of shrinkage, indicating that densification sintering mechanisms were dominant. Similar to sintering at 1000°C however, there were two distinct groups of parts based on the amount of shrinkage seen. Samples CT-AH ○●●, CT-BH ○○● and CT-CH ○●○ had densification values of 10.2%, 13.9% and 22.6% respectively, while samples CT-DH ●○● and CT-EH ●●○ had densification values of 31.6% and 38.6%. The 1400°C sintering treatment brought samples CT-AH ○●●, CT-BH ○○● and CT-CH ○●○ either close to, or just above the 70% theoretical density threshold that indicates the samples progressed into the intermediate stage of sintering. This is also indicated by the sinter necks of the samples, shown in Figure 8, that are generally in the range of 1/3 to 1/2 the particle diameter.

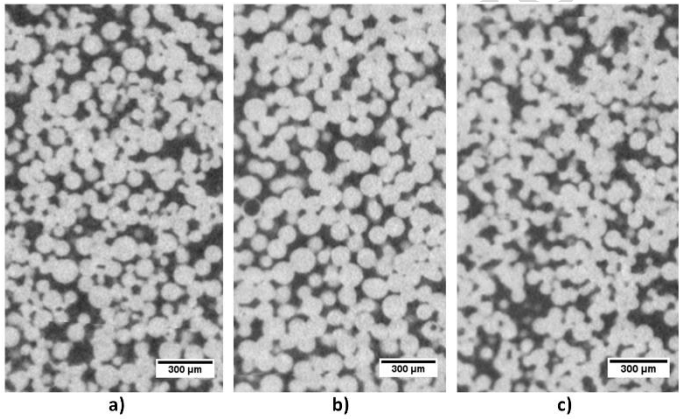

Figure 8: XZ plane cross-section images from reconstructed CT data of samples (a) CT-AH ○●●, (b) CT-BH ○○●, and (c) CT-CH ○●○ in the sintered state showing a qualitative view of the sample sinter necks between particles in the ROI

Even though all of the samples (CT-AH ○●●, CT-BH ○○● and CT-CH ○●○) had similar final densities, sample CT-CH ○●○ shrunk considerably more than both CT-AH ○●● and CT-BH ○○●, having nearly double the shrinkage. This substantial increase in densification is due to the higher driving force for sintering seen for the 45-106 µm particles. This demonstrates that using smaller, but not necessarily ultra-fine, powder still gives tangible improvements in terms of densification. In addition, due to the smaller particle size, the Type C ○●○ powder can give better surface finish and feature resolution compared to the type A and B powders. Generally, the use of the Type C ○●○ powder can be beneficial if trying to achieve higher density, but potentially detrimental if trying to reduce shrinkage. To obtain any real benefit with the Type C ○●○ powder, the green density of the parts needs to be higher otherwise the sample will simply undergo more shrinkage to achieve a similar final density.

One unexpected aspect of the sinter results is that sample CT-BH ○○● shrunk somewhat more than CT-AH ○●●, even though CT-BH ○○● had the largest particle size composition. One reason for this could be due to the difference in green density and therefore the number of contact points in each powder system. From a qualitative view of cross-sections from samples CT-AH ○●● and CT-BH ○○● in the green state, see Figure 9, it appears that more of the particles in CT-BH ○○● are in direct contact with each other, compared to CT-AH ○●● where many of the particles have a slight gap between them, and hence no true contact points. As discussed earlier, a major driving force for sintering is the curvature of the particle system, which only exists if there are contact points. This difference in contact points and driving force for sintering could explain the difference in shrinkage results. However, one would expect that since Type B ○○● powder had higher levels of shrinkage when sintered at 1400°C, it would also see it at 1000°C, which is not the case. It could be that the Type B ○○● powder was able to take advantage of the larger driving force when sintered at 1400°C but not at 1000°C. It should be noted that the difference in density could simply be attributed to the specific ROI that was sampled or variation in the samples themselves.

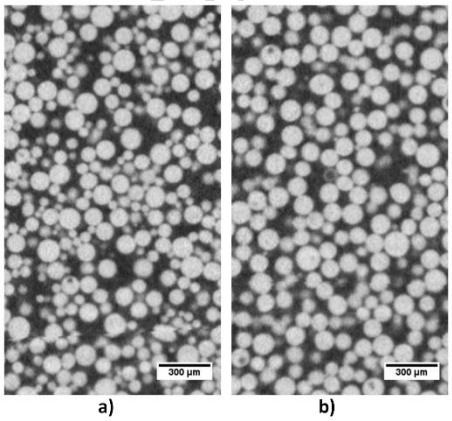

Figure 9: XZ plane cross-section images from reconstructed CT data of samples (a) CT- AH ○●● and (b) CT-BH ○○● in the green state showing a qualitative view of the sample contact points between particles in the ROI

Samples CT-DH ●○● and CT-EH ●●○ make up the second group and were sintered well past the 70% theoretical density threshold expected for this sintering regime, with considerably more densification than the other samples. These results were generally expected due to the higher driving force seen in the finer (0-45 µm) particles. While the parts as a whole did not technically enter into the final phase of sintering, localized areas within the samples did. This was confirmed with subsequent density analysis done as a function of height and shown later on.

Even without the image analysis, the localized density differences are large enough that they can be seen visually in Figure 10, where areas that had high concentrations of the finer particles are now almost fully dense. Areas occupied by the larger particles still have more significant amounts of remaining porosity. In addition, the individual small particles in these regions are indistinguishable from each other. This indicates that the sinter necks are larger than the 1/2 particle diameter threshold, also indicating the final stage of sintering. The results from the CT analysis indicate that if the 0-45 µm powder can be successfully printed on its own, it is likely that parts could be sintered into the 90% dense range. It is important to note that the high density that was achieved came at a cost of large levels of shrinkage. While samples CT-DH ●○● and CT-EH ●●○ achieved the highest final density, they also had the lowest green densities.

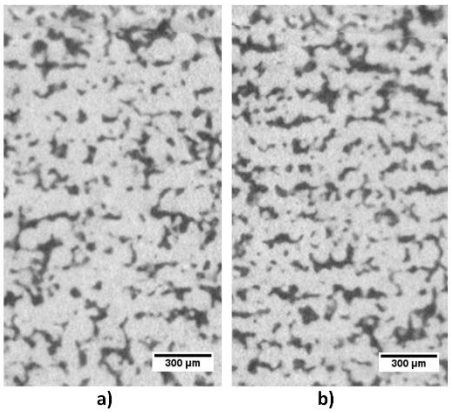

Figure 10: XZ plane cross-section images from reconstructed CT data of samples (a) CT-DH ●○● and (b) CT-EH ●●○ in the sintered state showing a qualitative view of the sample sinter necks between particles in the ROI

3.2 Relation between Density and Localized Particle Distribution

From the relative bulk density analysis above, samples were categorized into two groups based on sintering behavior, the first group having samples with powder Type A ○●●, B ○○●, and C ○●○, and the second group with powders Type D ●○●, and E ●●○.

As a representative behavior for parts in the first category, the part density and particle distribution maps for the Type B ○○● samples are shown in Figure 11 for a 1.25mm x 1.25mm x 2.25mm xyz ROI in the green and sintered states for both densifying (H) and non-densifying (L) regimes; Type A ○●● and C ○●○ shown in Data in Brief. The green and sintered density for both densifying (Figure 11a-i) and non-densifying (Figure 11a-ii) regimes show fluctuations with a period equivalent to the layer thickness (150 µm). For the densifying regime, (Figure 11a-i),

the relative density simply shifts to a higher average value after sintering without significant dampening of fluctuations, while for the non-densifying regime, (Figure 11a-ii), there is virtually no visible change in the density profile. The particle size distribution throughout Type B ○○● parts is consistent between the green states shown in Figure 11 (b-i, b-ii) and sintered states (Figure 11c-i, c-ii). However, for the densifying regime, most of the particles < 50 µm present in the green state (Figure 11b-i), do not appear in the sintered state (Figure 11c-i), as these particles likely progressed through densification sintering. There is an oscillation between zones with higher presence of larger particles and zones with smaller particles along the z-axis. The particles maps, correlated with the density profiles, show that the areas with more of the larger particles have a higher density, while those with more of the smaller particles have a lower density.

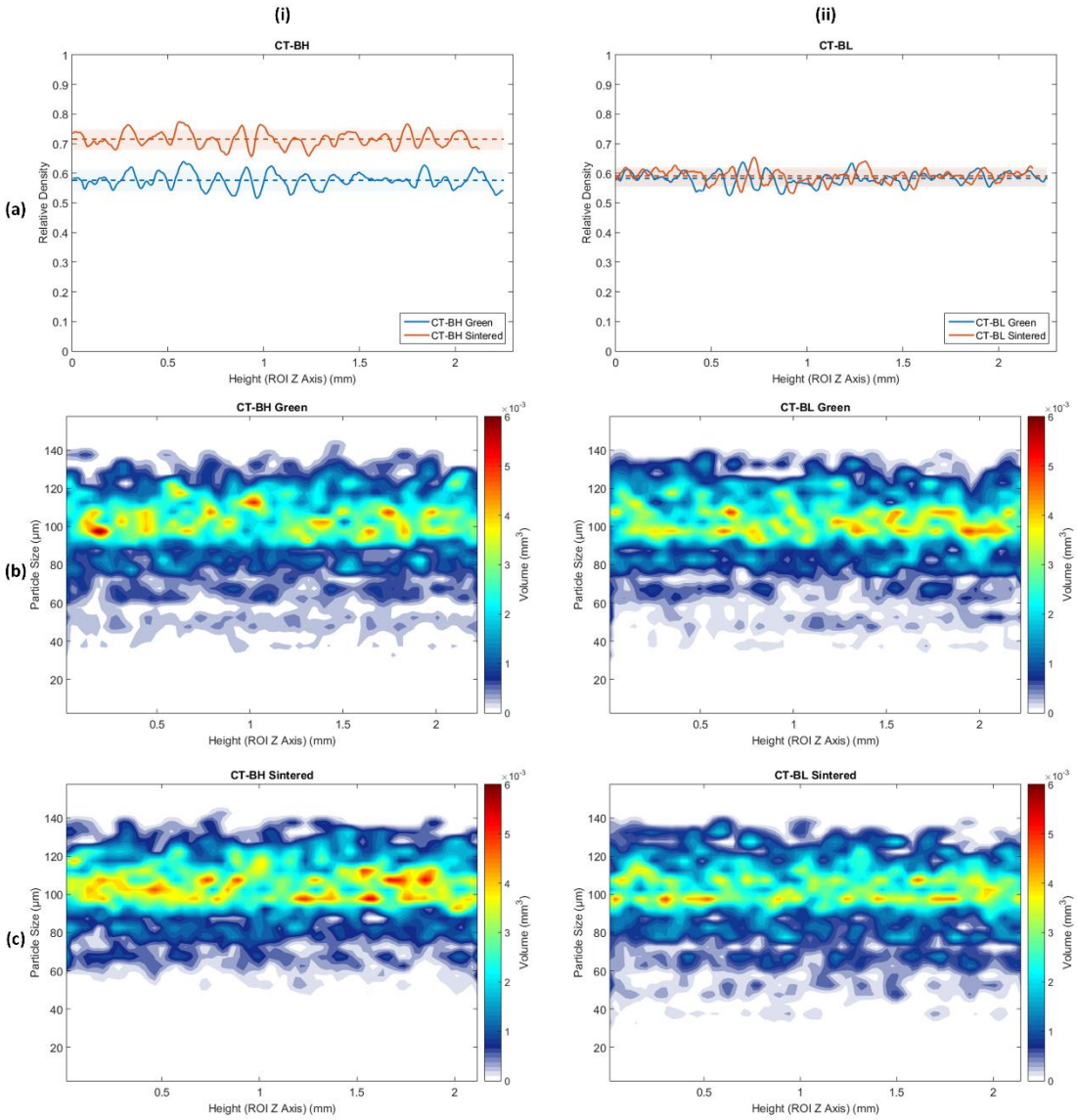

Figure 11: Density and particle size as a function of height for the Type B ○○● powder samples in the green and sintered state for densifying (H) and non-densifying (L) regimes. (a-i) relative density of the part before and after sintering for densifying (H) sintering and (a-ii) non-densifying sintering (H) respectively. (b-i, ii) and (c-i, cii) is the particle size (µm) and the corresponding volume fraction (mm^3) belonging to each particle size per CT layer for the green and sintered states respectively.

The effects of regions of small and large particles segregation are even more explicit in the Type D ●○● and Type E ●●○ powder samples, with the representative results for the CT-EH ●●○ sample in its green state shown in Figure 12. Upon closer inspection of this representative figure, it can be seen that in the green state of parts using Type E ●●○ powders, there are distinct periodic areas along the Z axis with a concentration of fine particles and almost a complete lack of the larger particles, followed by a segment of segregated large particles. This sequence of zones of small and large particle agglomerations is consistent throughout the entire part ROI. This periodicity in the green part is expected to result in distinct non-homogeneity after sintering.

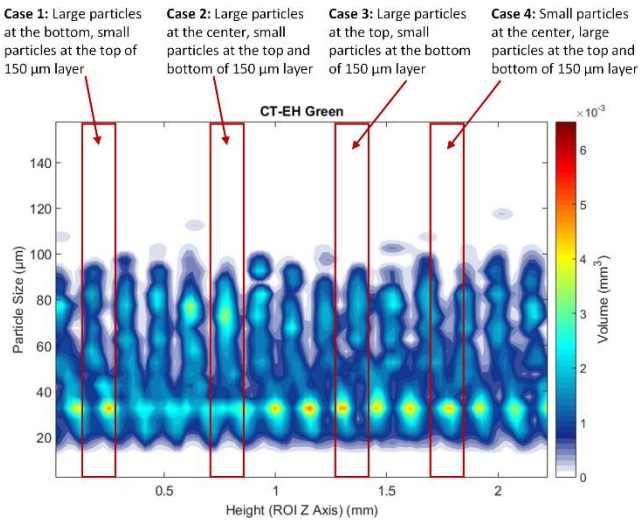

Figure 12: Particle map for sample CT-EH ●●○ in the green state, with highlighted 150 µm (layer thickness) segments indicating all the possible cases of particle segregation with respect to location within the layer

The relative density and particle size maps of Type D ●○● samples in the green state and sintered (densifying and non-densifying) state as shown in Figure 13. It can be observed that the density of the parts follows a periodic fluctuation, with the highest density corresponding to areas with larger particles and the lowest density to zones with the smaller particles. Data registration of particle size maps with part density along the z-axis in the sintered state was more difficult to achieve, however the density followed the same periodic trend. A similar trend is seen in Type E ●●○ samples showcased in the Data in Brief.

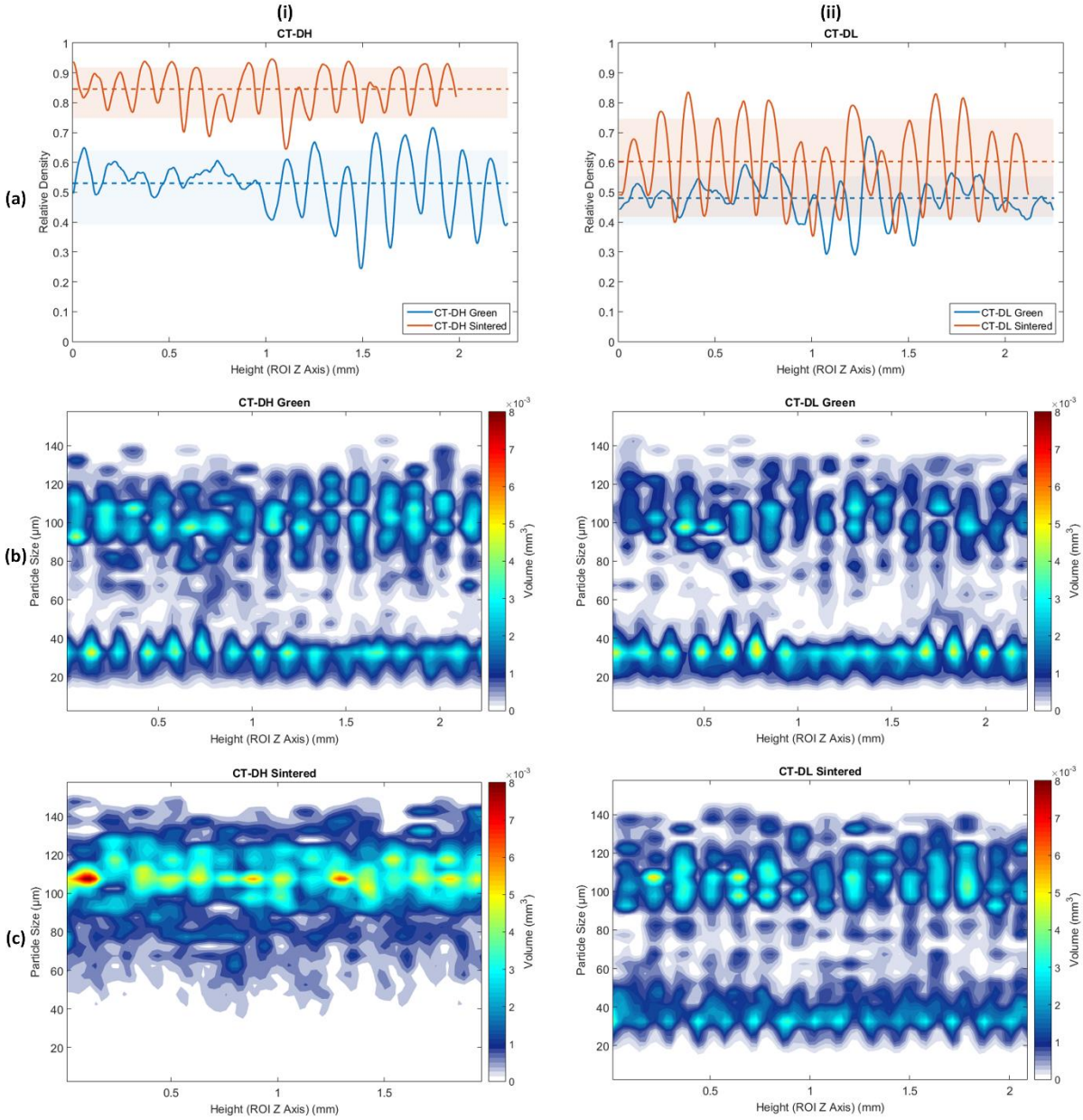

Figure 13: Density and particle size as a function of height for the Type D ●○● powder samples in the green and sintered state for densifying (H) and non-densifying (L) regimes. (a-i) relative density of the part before and after sintering for densifying (H) sintering and (a-ii) non-densifying sintering (H) respectively. (b-i, ii) and (c-i, cii) is the particle size (µm) and the corresponding volume fraction (mm^3) belonging to each particle size per CT layer for the green and sintered states respectively.

Due to the consistent periodic nature of particle size segregation, and the fact that segregation only occurs in the Z axis, the effect undoubtedly is caused by and during the printing process. Particle segregation occurred more drastically in blends containing the 0-45 µm powder. One cause may be that particle blends were not properly homogenized before printing, and that

carried over into the build bed. A lack of homogenization of the bulk powder, however, does not explain the periodic nature of the variation, nor the orientation with respect to the build direction.

Another probable explanation for the particle segregation effect is due to the compaction process during powder spreading. When the counter-rotating roller passes over the build bed, the larger particles are inherently forced down into the powder bed. This could potentially displace the smaller particles, causing the stratification in particle size. Even with particles being pushed in, either by the roller or the previous layer resisting compaction, the particles cannot displace the entire layer, only a fraction of it. One would then expect to still see a relatively homogeneous mix of large and small particles, which is not the case in the observed samples.

Another cause of the particle segregation is the dynamics of spreading. Due to the counter-rotating roller, the powder is highly agitated as it is spread. While the spreading time is relatively short, the distance over which the powder needs to segregate during spreading is quite small, of a similar order of magnitude as the layer thickness. This could reasonably allow the powder to segregate during spreading. This aspect should be investigated further to determine whether the segregation is only caused by the spreading mechanism.

Another viable cause of particle segregation could be attributed to liquid jetting. When binder is jetted from the print head, it impacts the powder surface at high velocity. The droplet impact and fluid imbibition could provide enough force to dislodge smaller particles downward. In this study, a thermal inkjet HP10 print head with a droplet size of 10-80 pL was used. In-depth studies of the interaction between the liquid binder and powder substrates as a function of powder size [51,52] focused on predicting or observing liquid infiltration, rather than on particle migration due to liquid interactions. Droplet kinetics and gravity have been assumed negligible for a ~54 μm droplet size (~80 pL) [51] to simplify modeling of fluid imbibition. In light of the current observations, a more careful consideration of these assumptions should be considered.

A final proposed cause of the fine particle segregation is due to fine particles preferentially sticking to the wet surface of the previously wetted layer during spreading. As a powder front precedes the roller before the roller is overtop of the wetted area, finer particles may preferentially adhere to the wet substrate ahead of the roller compacting the powder layer. This could cause a non-uniform buildup of the finer particles the bottom of the layer, causing the

effective particle segregation. While this would explain a build-up of smaller particles at the layer interfaces, it still does not fully explain the particle segregation within the spread layers.

Regardless of the root cause, this segregation between the large and small particles types goes towards explaining the shift in the density profiles for all of the powder samples, as discussed later. This phenomenon will be the focus of a future study, where the authors look to decouple the effects of the powder spreading mechanism and liquid permeation on the powder size intra and inter-layer segregation. A visualization of such a segregation is seen in Figure 14, for a Type D ●○● green part and a Type B ○○● green part respectively. The particle segregation for Type D ●○● is visible, with a distinct sequence of larger and smaller particle regions.

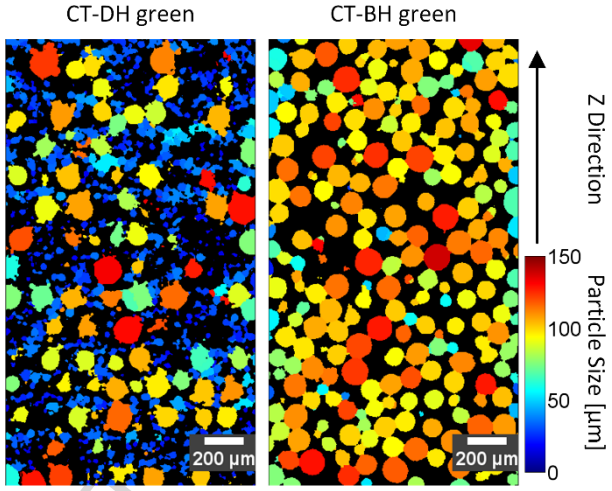

Figure 14 Particle segregation along the build direction for Type D ●○● and Type B ○○● green parts respectively. The scale shows the color binning for the particle size (µm).

3.3 Localized Relative Density

From the CT scan data, all parts were found have the density fluctuating with a spatial period equivalent to the layer thickness of 150 µm. Though all samples followed this trend, there were two distinct groups. Parts from powder Type A ○●●, Type B ○○● and Type C ○●○ showed lower relative density amplitude changes while those made with Type D ●○● and Type E ●●○ showed higher relative density amplitude fluctuations. The average amplitude of the density fluctuation is summarized in Table 6. It is important to note that neither densifying nor non-densifying sintering methods eliminated the fluctuation in density, resulting in parts with anisotropic properties. Even though the anisotropy is present, the density fluctuation is relatively small for the first group of samples, meaning the difference in properties is also relatively small.

The second group of samples, Type D ●○● and Type E ●●○, show a higher amplitude of the density profile. This difference in densification is due the observed segregation of the smaller and larger particles and the corresponding difference in contact points and driving force for sintering. With more contact points and generally a higher driving force for sintering in areas with the larger number of fine particles, densification should preferentially occur there. As the areas with the fine particles densify, the adjacent larger particles will be pulled into those areas as well, potentially breaking sinter necks or contact points between the larger particles that sinter at comparatively slower rates. This effect, if present, is likely only significant with the powder types with finer particles since they sinter at significantly lower temperatures, allowing necks and shrinkage to occur before the larger particles can sinter to any appreciable amount.

Table 6: Summary of the mean high and mean low relative density ranges for the samples in both the green and sintered state, in densifying sintering (H) and non-densifying sintering (L) regimes

Sample Name	Green Density Mean High (%)	Green Density Mean Low (%)	Green Density Fluctuation Range (%)	Sintered Density Mean High (%)	Sintered Density Mean Low (%)	Sintered Density Fluctuation Range (%)
CT-AL ○●●	60.1 ± 2.9	48.9 ± 3.0	**11.2**	64.4 ± 3.2	50.4 ± 2.9	**14.0**
CT-AH ○●●	61.9 ± 3.3	47.1 ± 3.2	**14.8**	71.3 ± 3.1	57.6 ± 3.1	**13.7**
CT-BL ○○●	61.3 ± 1.3	55.4 ± 1.7	**5.8**	62.0 ± 1.5	55.6 ± 1.5	**6.4**
CT-BH ○○●	61.1 ± 1.6	54.0 ± 1.4	**7.1**	74.8 ± 1.8	68.0 ± 1.3	**6.8**
CT-CL ○●○	54.6 ± 3.3	45.6 ± 1.9	**8.9**	58.8 ± 2.8	49.8 ± 1.5	**9.0**
CT-CH ○●○	53.2 ± 3.0	43.7 ± 1.5	**9.5**	75.9 ± 2.9	65.6 ± 1.7	**10.2**
CT-DL ●○●	55.4 ± 5.4	39.1 ± 6.7	**16.2**	74.6 ± 6.8	41.8 ± 4.0	**32.9**
CT-DH ●○●	64.0 ± 4.6	39.3 ± 8.4	**24.7**	91.8 ± 2.8	74.9 ± 4.5	**16.9**
CT-EL ●●○	62.9 ± 5.5	28.9 ± 4.4	**34.0**	73.4 ± 5.2	40.9 ± 5.9	**32.5**
CT-EH ●●○	54.5 ±7.1	37.3 ± 5.0	**17.2**	92.9 ± 1.7	68.8 ± 3.8	**24.1**

3.4 Overall Effective Particle Size

While effective particle size cannot be used to directly identify specific part properties, it is indicative as to the degree of sintering that occurred within the parts. If a part is sintered at low temperatures, and minimal densification and neck formation occurs, then there should also be a minimal change in detected particle size via CT after sintering. If sintered at high temperatures, there should be a larger change in measured particle size as necks grow and particles converge together. The mean particle sizes measured using CT for the parts in both the green and sintered state are summarized in Table 7. The corresponding histogram plots for particle size distributions for powder Type A ○●●, C○●○, and E ●●○ are illustrated in the Data in Brief. Representative histograms for Type B ○○● and Type D ●○● are shown in Figure 15 and Figure 16 respectively.

Table 7: Summary of sample mean effective particle sizes in the green and sintered state for densifying (H) and non-densifying (L) regimes

Sample Name	Mean Particle Size (µm)		
	Green	Sintered	Change
CT-AL ○●●	55.4	55.6	0.2
CT-AH ○●●	60.4	67.5	7.1
CT-BL ○○●	82.7	81.8	-0.9
CT-BH ○○●	82.1	90.8	8.7
CT-CL ○●○	54.7	53.8	-0.9
CT-CH ○●○	54.5	68.3	13.8
CT-DL ●○●	27.0	31.2	4.2
CT-DH ●○●	28.8	78.9	50.1
CT-EL ●●○	27.5	35.3	7.8
CT-EH ●●○	28.9	72.4	43.5

Similar to the results seen for porosity, the parts can be grouped based on the sintering temperature and whether fine particles were added into the powder mixture. The parts with only larger particles and sintered at 1000°C (CT-AL ○●●, CT-BL ○○● and CT-CL ○●○), with the representative Figure 15(b) showing the Type B ○○● powder samples sintered at low 1000 °C temperature (CT-BL ○○●), had effectively no change in mean particle size, as was expected. This was due to the limited neck formation and minimal densification. Parts with the same powder types but sintered at 1400°C (CT-AH ○●●, CT-BH ○○● and CT-CH ○●○) had a more significant change in mean effective particle size, due to the more significant neck formation seen in these parts. A representative behavior is shown in Figure 15(a) for CT-BH ○○●.

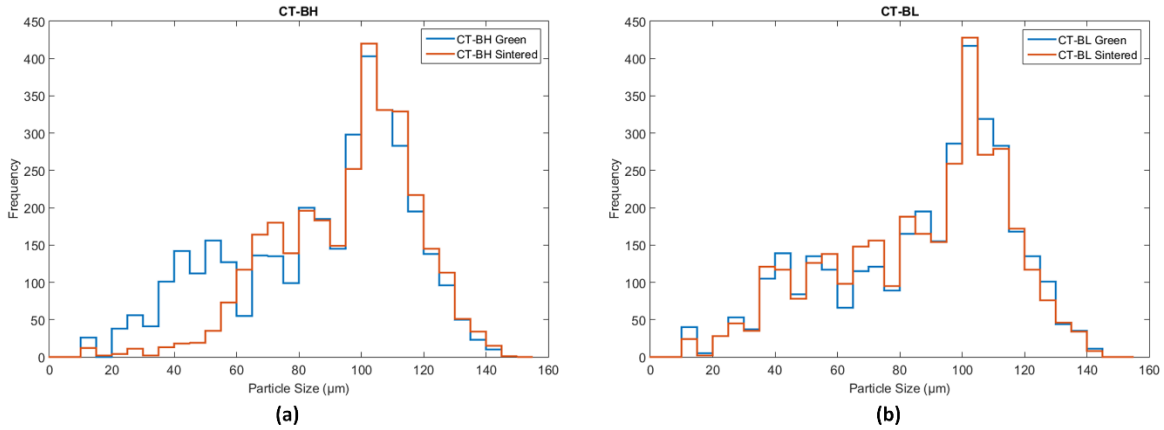

Figure 15: Overall particle size histogram of the Type B ○○● powder samples in the green and sintered state for (a) densifying (H) and (b) non-densifying (L) regimes

The parts produced using powder types containing the smallest particle range (0-45 µm) had a more significant increase in effective particle size detected after sintering compared to

those comprised of only larger particles. Even the samples sintered at 1000°C (CT-DL ●○● and CT-EL ●●○), were found to have a larger proportional increase in particle size, with the representative Type D ●○● powder sown in Figure 16 (b). This is due to the proportionally larger sinter necks seen with the smaller particles even when sintered at the lower temperatures. Parts sintered at 1400°C (CT-DH ●○● and CT-EH ●●○) have a larger change in mean particle size, with the value nearly doubling, with the representative Type D ●○● sown in Figure 16 (a). The substantial change is due to the small particles entering the final stage of sintering with localized areas becoming nearly fully dense, thus measured as larger particles, contributing to an increase in the mean particle size. The areas of near full density remove the contribution of the finer particles to the overall measured distribution.

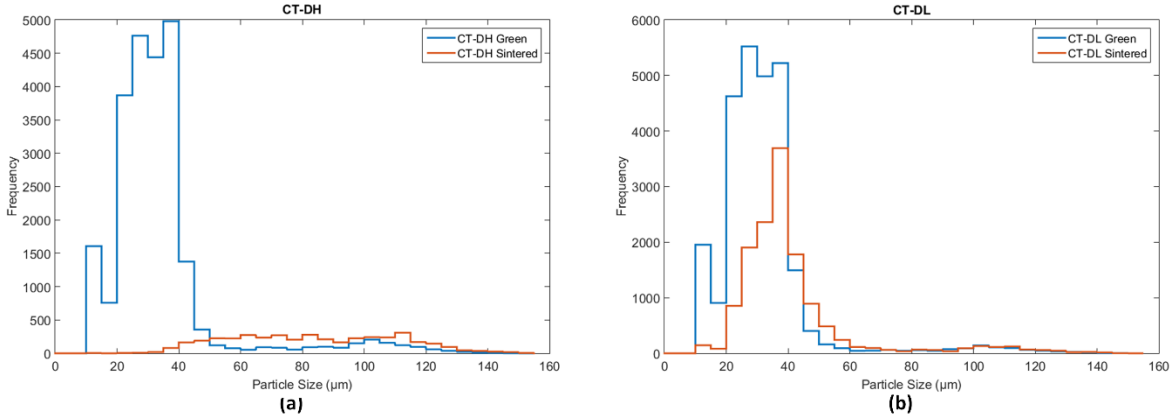

Figure 16: Overall particle size histogram of the Type D ●○● powder samples in the green and sintered state for (a) densifying (H) and (b) non-densifying (L) regimes

3.5 Overall Effective Pore Size

The mean pore size results of the samples in both the green and sintered state are summarized in Table 8. Similarly, the samples can be split into two groups.

Table 8: Summary of sample mean pore sizes in the green and sintered state for densifying (H) and non-densifying (L) regimes

	Mean Pore size (μm)		
Sample Name	Green	Sintered	Change
CT-AL ○●●	38.8	37.8	-1.0
CT-AH ○●●	42.6	40.0	-2.6
CT-BL ○○●	45.4	44.2	-1.2
CT-BH ○○●	46.0	37.6	-8.4
CT-CL ○●○	40.5	38.3	-2.2
CT-CH ○●○	42.6	36.5	-6.1
CT-DH ●○●	29.7	24.6	-5.1
CT-DL ●○●	31.7	29.1	-2.6

CT-EL ●●○	30.1	27.8	-2.3
CT-EH ●●○	31.4	25.2	-6.2

Samples made from powders Type A ○●●, B ○○● and C ○●○ all show a single mode distribution of pore size, with a peak ~ 40µm. The corresponding histogram plots for the pore sizes distributions of Type A ○●● and C ○●○ are illustrated in the Data in Brief. Samples sintered at 1000°C had effectively no change in pore size and number of pores after sintering, with Type B ○○● shown in Figure 17 (b). Since these parts predominantly remained in the initial sintering stage, neck sizes are comparatively small, meaning the pore sizes would not be affected significantly. Samples in this category sintered at 1400°C had a larger decrease in pore size and pore count, though the change is still relatively small, with a representative behavior shown for Type B ○○● in Figure 17 (a).

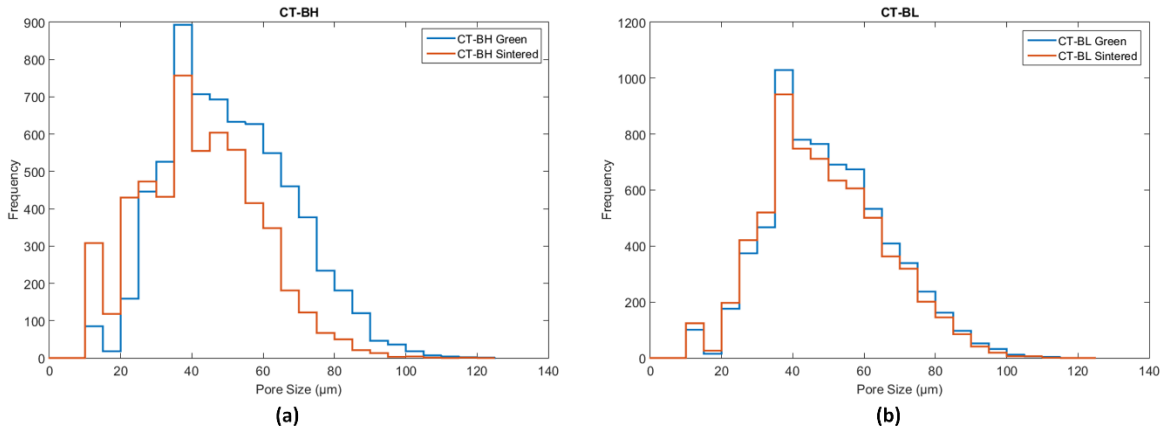

Figure 17 Overall pore size histogram of the Type B ○○● powder samples in the green and sintered state for (a) densifying (H) and (b) non-densifying (L) regimes

Samples made with powder Types D ●○● and E ●●○, show a bimodal pore size distribution. This can be seen for the Type D ●○● powder samples in Figure 18, with peaks around 10µm and 40µm. The corresponding histogram plots for the pore sizes distributions of Type E ●●○ are illustrated in the Data in Brief. It should be noted that due to the voxel size used during scanning, only pores with a diameter of 10µm or larger can be reliably detected. Samples in the second group sintered at 1400°C (CT-DH ●○●, CT-EH ●●○) show a significant change in pore distribution, with a significant portion of the larger pores being lost, as seen in Figure 18 (a). This is likely due to the more significant levels of shrinkage seen with these parts compared to the other category of samples, supporting the idea that small particles enter the final stage of sintering.

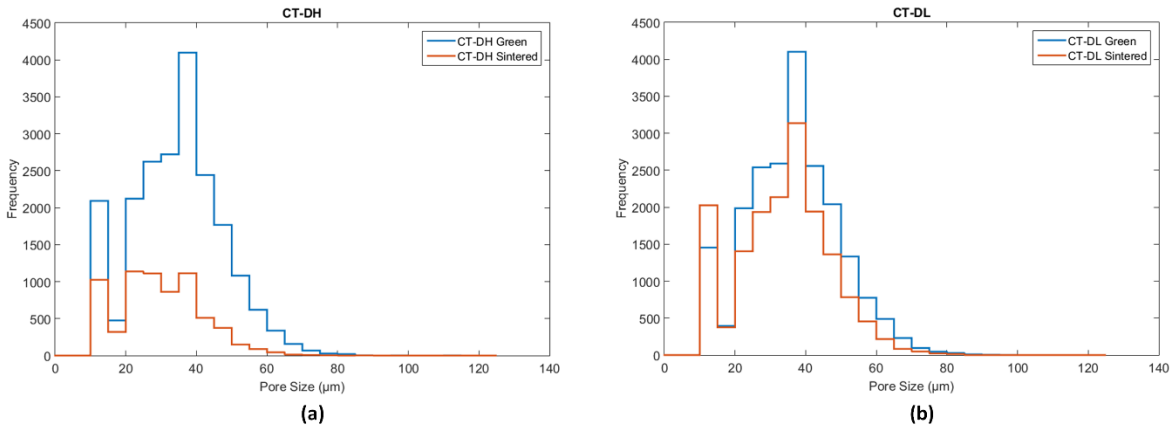

Figure 18 Overall pore size histogram of the Type D ●○● powder samples in the green and sintered state for (a) densifying (H) and (b) non-densifying (L) regimes

Pore elimination, and therefore a substantial change in pore size, only occurs in the final stage of sintering [36]. The parts as a whole remained within the intermediate stage of sintering meaning only the general pore network structure was altered. As discussed earlier the pore network is still interconnected, but becomes more tubular during the intermediate stage as sinter necks grow. While this does change the general structure, it had a minimal effect on the actual pore diameters [37]. For a more substantial change in pore size to be seen, parts would have to progress further into the final stage of sintering where pores are isolated and eliminated.

3.6 Sinter Neck Size

Due to the voxel size the parts were scanned at, sinter neck sizes below 50µm could not be reliably detected, and cannot be used in calculations for sinter neck statistics. This is problematic since the sinter necks are expected to be significantly small, especially for the blends containing the finer particles (0-45µm). It was decided that, due to the large gap in reliable measurements, only a qualitative inspection of sinter necks from cross-sections of the CT data would be made.

4 Conclusion

The first conclusion that can be made as part of the sinter structure analysis is that CT is a viable and useful technique for measuring the properties of BJAM parts. The results from the CT analysis showed both bulk properties as well as properties on a per-layer basis, in both the green

and sintered state. While there was a limitation on measuring sinter necks and pores below 50 µm and 10 µm respectively, the method provided insightful sinter structure information.

The second conclusion that can be made is that the addition of finer particles improves the bulk density of sintered parts, but at the cost of higher levels of shrinkage. The addition of finer particles decreases green part density, but the higher driving force for sintering compensates for this, allowing the parts to achieve fairly high density levels, around 85%. The large amount of shrinkage seen with these parts, on the order of 40%, would make it difficult to create compensation values for small, complex features.

The third conclusion that can be made is that the BJAM parts have high levels of density variation through the build height. Parts made with the larger powder blends (Types A ○●●, B ○○● and C ○●○) showed the least amount of green density variation, approximately ± 8% around the mean. Parts made with the fine powder blends (Types D ●○● and E ●●○) show very high levels of density fluctuations with green density fluctuating approximately ± 20% around the mean. This high level of fluctuation in density means that although parts with the finer particles have a higher sintered bulk density, they result in higher levels of anisotropy.

The fourth conclusion that can be made is that segregation of particles occurs during the printing process. The possible causes of this effect are the counter-rotating roller used in the BJAM system, which causes a significant agitation of the powder as it is being spread, and the interaction between the liquid binder and the powder. However, the relation between these causes and the segregation effects requires further exploration to make definitive statements.

Acknowledgments

The authors appreciate the support received from prof. Toyserkani in supporting this research. The authors appreciate the efforts of Phil Meszaros, Research Associate in the Multi-Scale Additive Manufacturing Laboratory, in helping to visualize data for this study.

Data Availability

The raw and processed data required to reproduce these findings cannot be shared at this time due to technical limitations related to file size for CT files. Data is available upon request.

5 References

[1] T. Wohlers, 3D Printing and Additive Manufacturing State of the Industry, in: Wohlers Rep. 2017, Wohlers Associates, 2017.

[2] C. Lindemann, U. Jahnke, M. Moi, R. Koch, Analyzing product lifecycle costs for a better understanding of cost drivers in additive manufacturing, Int. Solid Free. Fabr. Symp. 23 (2012) 177–188. doi:10.1007/s13398-014-0173-7.2.

[3] T. Douglas, S. Gilvert, Costs and Cost Effectiveness of Additive Manufacturing, NIST Spec. Publ. (2014). doi:10.6028/NIST.SP.1176.

[4] U.S. Patent, S. Haggerty, J. Michael, P.A. Williams, Three-Dimensional Printing Techniques, 5.204.055, 1993.

[5] E. Sachs, S. Allen, M. Cima, E. Wylonis, H. Gu, Production of Injection Molding Tooling With Conformal Cooling Channels Using the Three Dimensional Printing Process Production of Injection Molding Tooling with Conformal Cooling Channels using The Three Dimensional Printing Process, Polym. Eng. Sci. 40 (2000) 1232–1247. doi:10.1002/pen.11251.

[6] M. Ziaee, E.M. Tridas, N.B. Crane, Binder-Jet Printing of Fine Stainless Steel Powder with Varied Final Density, Jom. 69 (2017) 592–596. doi:10.1007/s11837-016-2177-6.

[7] S. Shrestha, G. Manogharan, Optimization of Binder Jetting Using Taguchi Method, Jom. 69 (2017) 491–497. doi:10.1007/s11837-016-2231-4.

[8] B. Zhang, Z. Zhan, Y. Cao, H. Gulan, P. Linnér, J. Sun, T. Zwick, H. Zirath, Metallic 3-D Printed Antennas for Millimeter- and Submillimeter Wave Applications, IEEE Trans. Terahertz Sci. Technol. 6 (2016) 592–600. doi:10.1109/TTHZ.2016.2562508.

[9] T. Do, P. Kwon, C.S. Shin, Process development toward full-density stainless steel parts with binder jetting printing, Int. J. Mach. Tools Manuf. 121 (2017) 50–60. doi:10.1016/j.ijmachtools.2017.04.006.

[10] A. Mostafaei, Y. Behnamian, Y.L. Krimer, E.L. Stevens, J.L. Luo, M. Chmielus, Effect of solutionizing and aging on the microstructure and mechanical properties of powder bed binder jet printed nickel-based superalloy 625, Mater. Des. 111 (2016) 482–491. doi:10.1016/j.matdes.2016.08.083.

[11] A. Mostafaei, E.L. Stevens, E.T. Hughes, S.D. Biery, C. Hilla, M. Chmielus, Powder bed binder jet printed alloy 625: Densification, microstructure and mechanical properties,

Mater. Des. 108 (2016) 126–135. doi:10.1016/j.matdes.2016.06.067.

[12] A. Mostafaei, J. Toman, E.L. Stevens, E.T. Hughes, Y.L. Krimer, M. Chmielus, Microstructural evolution and mechanical properties of differently heat-treated binder jet printed samples from gas- and water-atomized alloy 625 powders, Acta Mater. 124 (2017) 280–289. doi:10.1016/j.actamat.2016.11.021.

[13] M.P. Paranthaman, C.S. Shafer, A.M. Elliott, D.H. Siddel, M.A. McGuire, R.M. Springfield, J. Martin, R. Fredette, J. Ormerod, Binder Jetting: A Novel NdFeB Bonded Magnet Fabrication Process, Jom. 68 (2016) 1978–1982. doi:10.1007/s11837-016-1883-4.

[14] L. Li, B. Post, V. Kunc, A.M. Elliott, M.P. Paranthaman, Additive manufacturing of near-net-shape bonded magnets: Prospects and challenges, Scr. Mater. 135 (2017) 100–104. doi:10.1016/j.scriptamat.2016.12.035.

[15] A. Basalah, Y. Shanjani, S. Esmaeili, E. Toyserkani, Characterizations of additive manufactured porous titanium implants, J. Biomed. Mater. Res. - Part B Appl. Biomater. 100 B (2012) 1970–1979. doi:10.1002/jbm.b.32764.

[16] E. Sheydaeian, E. Toyserkani, A system for selectively encapsulating porogens inside the layers during additive manufacturing: From conceptual design to the first prototype, J. Manuf. Process. 26 (2017) 330–338. doi:10.1016/j.jmapro.2017.03.001.

[17] Y. Bai, C.B. Williams, An exploration of binder jetting of copper, Rapid Prototyp. J. 21 (2015) 177–185. doi:10.1108/RPJ-12-2014-0180.

[18] P. Stoyanov, K. Andre, P. Prichard, M. Yao, C. Gey, Microstructural and Mechanical Characterization of Mo-containing Stellite Alloys Produced by three Dimensional Printing, Procedia CIRP. 45 (2016) 167–170. doi:10.1016/j.procir.2016.02.358.

[19] ExOne, Casting Media Alternatives, (2015).

[20] M. Materials, T. Data, F.O.R. Sand, Material data sheet for Furan-Direct-Binding (FDB) sand molds, (n.d.) 1–2.

[21] J.A. Gonzalez, J. Mireles, Y. Lin, R.B. Wicker, Characterization of ceramic components fabricated using binder jetting additive manufacturing technology, Ceram. Int. 42 (2016) 10559–10564. doi:10.1016/j.ceramint.2016.03.079.

[22] M.J. Cima, J. Yoo, S. Khanuja, M. Rynerson, D. Nammour, B. Giritlioglu, J. Grau, E.M. Sachs, Sturctural Ceramic Components by 3D Printing, Solid Free. Fabr. Symp. (1993) 479–488.

[23] L. Ferrage, G. Bertrand, P. Lenormand, D. Grossin, B. Ben-Nissan, A review of the additive manufacturing (3DP) of bioceramics: Alumina, zirconia (PSZ) and hydroxyapatite, J. Aust. Ceram. Soc. 53 (2017) 11–20. doi:10.1007/s41779-016-0003-9.

[24] I. Gibson, D. Rosen, B. Stucker, Additive Manufacturing Technologies, in: Addit. Manuf. Technol., Second, 2015: pp. 1–498. doi:10.1007/978-1-4939-2113-3.

[25] L. Rabinskiy, A. Ripetsky, S. Sitnikov, Y. Solyaev, R. Kahramanov, Fabrication of porous silicon nitride ceramics using binder jetting technology, IOP Conf. Ser. Mater. Sci. Eng. 140 (2016) 12023. doi:10.1088/1757-899X/140/1/012023.

[26] S.M. Gaytan, M.A. Cadena, H. Karim, D. Delfin, Y. Lin, D. Espalin, E. MacDonald, R.B. Wicker, Fabrication of barium titanate by binder jetting additive manufacturing technology, Ceram. Int. 41 (2015) 6610–6619. doi:10.1016/j.ceramint.2015.01.108.

[27] C. Polzin, S. Spath, H. Seitz, Characterization and evaluation of a PMMA-based 3D printing process, Rapid Prototyp. J. 19 (2013) 37–43. doi:10.1108/13552541311292718.

[28] X. Xu, S. Meteyer, N. Perry, Y.F. Zhao, Energy consumption model of Binder-jetting additive manufacturing processes, Int. J. Prod. Res. 53 (2015) 7005–7015. doi:10.1080/00207543.2014.937013.

[29] B. Levine, A new era in porous metals: Applications in orthopaedics, Adv. Eng. Mater. 10 (2008) 788–792. doi:10.1002/adem.200800215.

[30] P.A. Banaszkiewicz, Porous-coated hip replacement. The factors governing bone ingrowth, stress shielding, and clinical results, Class. Pap. Orthop. 69 (2014) 51–55. doi:10.1007/978-1-4471-5451-8_12.

[31] M.H. Lee, K.B. Kim, J.H. Han, J. Eckert, D.J. Sordelet, High strength porous Ti–6Al–4V foams synthesized by solid state powder processing, J. Phys. D. Appl. Phys. 41 (2008) 105404. doi:10.1088/0022-3727/41/10/105404.

[32] H. Schiefer, M. Bram, H.P. Buchkremer, D. Stöver, Mechanical examinations on dental implants with porous titanium coating, J. Mater. Sci. Mater. Med. 20 (2009) 1763–1770. doi:10.1007/s10856-009-3733-1.

[33] I.M. Robertson, G.B. Schaffer, Some effects of particle size on the sintering of titanium and a master sintering curve model, Metall. Mater. Trans. A Phys. Metall. Mater. Sci. 40 (2009) 1968–1979. doi:10.1007/s11661-009-9894-1.

[34] A. Mostafaei, K.A. Kimes, E.L. Stevens, J. Toman, Y.L. Krimer, K. Ullakko, M.

Chmielus, Microstructural evolution and magnetic properties of binder jet additive manufactured Ni-Mn-Ga magnetic shape memory alloy foam, Acta Mater. 131 (2017) 482–490. doi:10.1016/j.actamat.2017.04.010.

[35] L. Le Guéhennec, A. Soueidan, P. Layrolle, Y. Amouriq, Surface treatments of titanium dental implants for rapid osseointegration, Dent. Mater. 23 (2007) 844–854. doi:10.1016/j.dental.2006.06.025.

[36] R.M. German, Thermodynamics of Sintering, in: Sinter. Adv. Mater., 2010: pp. 3–32.

[37] R.M. German, Coarsening in Sintering: Grain Shape Distribution, Grain Size Distribution, and Grain Growth Kinetics in Solid-Pore Systems, Crit. Rev. Solid State Mater. Sci. 35 (2010) 263–305. doi:10.1080/10408436.2010.525197.

[38] J.L. Johnson, R.M. German, Theoretical modeling of densification during activated solid-state sintering, Metall. Mater. Trans. A Phys. Metall. Mater. Sci. 27 (1996) 441–450. doi:10.1007/BF02648421.

[39] R.M. German, Sintering Simplified: Surface Area, Density, and Grain Size Relations, Mater. Sci. Forum. 835 (2016) 50–75. doi:10.4028/www.scientific.net/MSF.835.50.

[40] E. a. Olevsky, Theory of sintering: from discrete to continuum, Mater. Sci. Eng. R Reports. 23 (1998) 41–100. doi:10.1016/S0927-796X(98)00009-6.

[41] E. Eylon, F.H. Froes, Products, Properties and Selection: Nonferrous Alloys and Special-Purpose Materials, in: ASM Handb., 1990: pp. 647–660.

[42] Z.Z. Fang, H. Wang, Sintering of ultrafine and nanosized particles, in: Sinter. Adv. Mater., 2010: pp. 434–473. doi:http://dx.doi.org/10.1533/9781845699949.3.434.

[43] R.M. German, P. Suri, S.J. Park, Review: Liquid phase sintering, J. Mater. Sci. 44 (2009) 1–39. doi:10.1007/s10853-008-3008-0.

[44] L. De Jonghe, M. Rahaman, Sintering of Ceramics, in: Handb. Adv. Ceram., 2003: pp. 187–264. doi:10.1016/B978-012654640-8/50006-7.

[45] M. Qian, G.B. Schaffer, C.J. Bettles, Sintering of Titanium and Its Alloys, in: Sinter. Adv. Mater. Fundam. Process., 2010: pp. 324–355.

[46] M.N. Rahaman, Kinetics And Mechanisms of Densification, in: Sinter. Adv. Mater., 2010: pp. 33–64.

[47] R.P. Elliott, Diffusion in Titanium and Titanium Alloys: Technical Documentary Report NO. ASD-TDR-62-561, 1962.

[48] W.D. Kingery, M. Berg, Study of the initial stages of sintering solids by viscous flow, evaporation-condensation, and self-diffusion, J. Appl. Phys. 26 (1955) 1205–1212. doi:10.1063/1.1721874.

[49] J. Hinebaugh, A. Bazylak, Pore Network Modeling to Study the Effects of Common Assumptions in GDL Liquid Water Invasion Studies, ASME 10th Int. Conf. Fuel Cell Sci. Eng. Technol. (2012) 479–484.

[50] Y. Bai, G. Wagner, C.B. Williams, Effect of Bimodal Powder Mixture on Powder Packing Density and Sintered Density in Binder Jetting of Metals, 2015 Annu. Int. Solid Free. Fabr. Symp. 139 (2015) 62. doi:10.1017/CBO9781107415324.004.

[51] R.K. Holman, M.J. Cima, S.A. Uhland, E. Sachs, Spreading and infiltration of inkjet-printed polymer solution droplets on a porous substrate, J. Colloid Interface Sci. 249 (2002) 432–440. doi:10.1006/jcis.2002.8225.

[52] M. Vaezi, C.K. Chua, Effects of layer thickness and binder saturation level parameters on 3D printing process, Int. J. Adv. Manuf. Technol. 53 (2011) 275–284. doi:10.1007/s00170-010-2821-1.

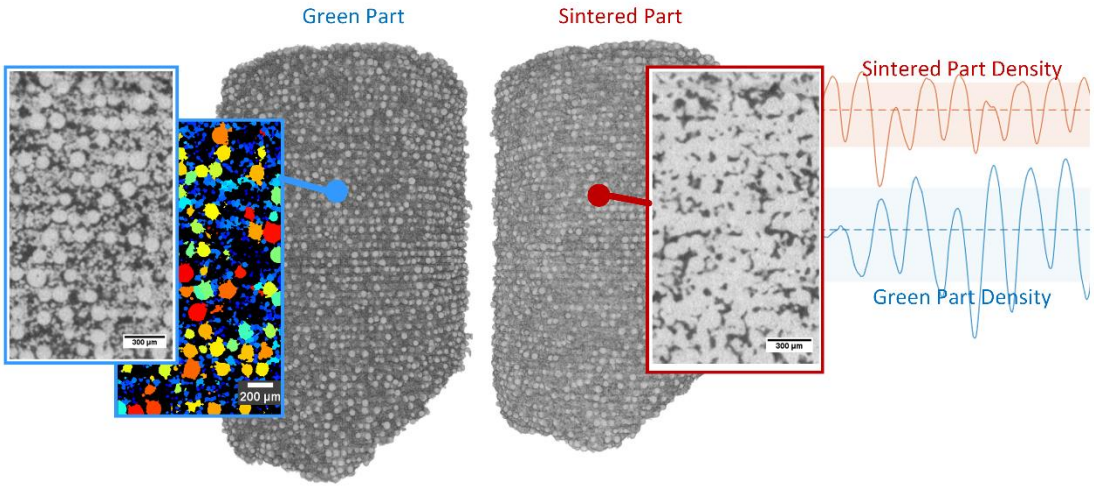

Graphical abstract

Highlights

- Computed tomography is necessary to evaluate per-layer properties of binder jet components
- Sintering temperature has a significant effect on density outcomes of binder jet components
- Both unimodal and bimodal powder blends produce anisotropic part characteristics
- Particle segregation occurs during the printing process and is the likely cause of anisotropy
- Finer particles increase sintered bulk density at the expense of high shrinkage and anisotropy